RSC Advances

PAPER

View Article Online
View Journal | View Issue

Cite this: *RSC Adv.*, 2026, **16**, 3111

Controllable synthesis and enhanced photochromic performance of Er-doped WO_3 nano neural network-like structures

Ran Tian,[b] Yu-Qiang An,*[b] Ze-Yuan Yang,*[a] Xing Yang[a] and Zhen-Hua Ge *[a]

Tungsten trioxide (WO_3) is a well-known photochromic material that undergoes a reversible color change under light irradiation, making it promising for applications in smart windows, optical storage, and sensing devices. This study presents the successful synthesis of a uniform and morphology-controlled WO_3 neural network-like structure by tuning the hydrothermal reaction temperature and hydrochloric acid concentration. Furthermore, the photochromic response time of the as-prepared WO_3 particles was systematically investigated, and the optimal sample exhibiting the fastest response was identified. To significantly enhance the photochromic performance, erbium (Er), a rare earth element, was introduced as a dopant. According to the results, Er doping significantly prolonged the photochromic response time of WO_3. The incorporation of Er led to a noticeable narrowing of the optical bandgap, as confirmed by UV-vis absorption and Tauc analysis. The $Er_{0.03}W_{0.97}O_3$ composition demonstrated superior performance compared to the other analyzed samples, indicating that the incorporation of rare earth elements can effectively regulate the photochromic behavior of WO_3 and provide a new pathway for tailoring its optical properties.

Received 13th August 2025
Accepted 6th January 2026

DOI: 10.1039/d5ra05957g

rsc.li/rsc-advances

Introduction

Photochromism refers to a reversible and persistent transformation between distinct states with different optical properties when exposed to excitation light.[1] Photochromic materials have garnered significant attention and are broadly classified into two main categories: organic compounds and inorganic materials (including transition metal oxides (TMOs), metal halides, and rare-earth complexes). Compared to organic photochromic materials, inorganic photochromic TMOs have drawn significant interest due to their excellent stability and cost-effectiveness.[2] The common photochromic TMOs include tungsten oxide (WO_3), molybdenum oxide (MoO_3), titanium dioxide (TiO_2), vanadium pentoxide (V_2O_5), niobium pentoxide (Nb_2O_5), and zinc oxide (ZnO).[3,4] When exposed to bandgap irradiation, TMOs can generate electron–hole pairs. Depending on the behavior of these photogenerated electrons and holes, the light absorption of TMOs can undergo significant changes after photoexcitation, resulting in observable color changes.[5]

Tungsten trioxide (WO_3) has garnered significant attention as a potential material for photochromic applications due to its ability to undergo reversible color changes following light irradiation.[6–8] Notably, the photochromic performance of WO_3 is strongly dependent on its microstructure and synthesis route.[9,10] Various fabrication techniques, including sol–gel, hydrothermal synthesis, chemical vapor deposition (CVD), and sputtering, have been extensively investigated to tailor their morphology and enhance their optical response.[11,12] These methods enable precise control over crystal size, surface area, and porosity, which are critical parameters influencing ion insertion/extraction dynamics and, consequently, the optical behavior of the material.[13] For instance, WO_3 nanostructures, which include nanoparticles, nanowires, and thin films, exhibit distinct photochromic and electrochromic properties, significantly affecting color contrast and switching kinetics.[14–16] This study focuses on the preparation techniques and morphological engineering of WO_3-based photochromic materials,[17,18] while exploring the relationship between microstructural characteristics and optical performance. Additionally, key challenges such as improving response speed, cycling stability, and the scalability of fabrication methods are discussed, along with prospects for the commercialization of WO_3-based photochromic systems.

To date, numerous researchers have reported on the research progress of WO_3-related photochromic materials.[15] For instance, in 2003, P. Leiderer *et al.*[16] extensively studied the photochromism of MoO_3 and discussed photochromism in TMOs. In 2006, Avellaneda *et al.*[19] reviewed the progress of photochromism in organic/inorganic composite materials based on TMOs (including WO_3-based photochromic materials) and multi-oxo metal esters. Furthermore, in 2010, Y. Badour *et al.*[20] provided a brief review on the development of inorganic–organic hybrid photochromic materials, including metal

[a]*Faculty of Materials Science and Engineering, Kunming University of Science and Technology, Kunming, 650093, China. E-mail: yangzy@stu.kust.edu.cn; zge@kust.edu.cn*

[b]*R & D Center of China Tobacco Yunnan Industrial Co., Ltd, Kunming 650032, China. E-mail: anyq@ynzy-tobacco.com*

halides, metal cyanides, polyoxo metal salts, metal chalcogenides, and metal–organic complexes. Recently, Wang *et al.*[21] published a review on the photocatalytic, electrochemical, and phototherapeutic applications of tungsten trioxide. Miyauchi *et al.*[22] reviewed the research progress on the coloration of WO_3 in energy-related applications. However, since 2010, only a few review articles have specifically discussed the photochromism of tungsten trioxide.[23] Currently, research on the doping modification of WO_3 primarily focuses on transition metal elements such as Ti, Mo, and Nb, which have demonstrated certain improvements in their photochromic performance.[24] However, studies on the effect of rare earth element doping on the photochromic behavior of WO_3 are relatively scarce. Rare earth elements possess abundant and unique energy level structures and are extensively utilized in luminescent materials, where electronic transitions and transfers occur under light excitation.[25] These electron transfer processes facilitate the valence state transformation between W^{6+} and W^{5+}, thereby enhancing the photochromic response of WO_3. Consequently, doping with rare earth elements holds significant potential to develop high-performance WO_3-based photochromic materials,[26] expanding their applicability in smart optical devices and information storage technologies.[27] In particular, WO_3-based photochromic materials hold great promise for practical applications such as smart windows with dynamic light and heat regulation, photocatalytic systems for environmental remediation, optical data storage, and next-generation optoelectronic devices. The ability to tailor their band structure and morphology through rare-earth doping provides new opportunities to further advance these applications.

In this study, uniform and morphology-controlled WO_3 nanoparticles were successfully synthesized by adjusting the hydrothermal reaction temperature and the concentration of hydrochloric acid in the system. The influence of synthesis conditions on the optical properties of WO_3 was systematically investigated, and the sample with the most favorable characteristics was identified. To further modulate the electronic structure, the rare earth element erbium (Er) was introduced as a dopant. The results demonstrate that Er doping effectively narrows the bandgap and enhances the visible-light absorption of WO_3, providing a promising strategy for tailoring its optical performance for photocatalytic and optoelectronic applications. Based on the available literature, this is the first report demonstrating that Er doping can induce the formation of neural network-like WO_3 nanostructures while simultaneously enhancing photochromic performance.

Experimental details

All reagents were analytical grade and used without further purification. Detailed synthesis procedures and variable definitions are as follows. Initially, 0.01 mol of sodium tungstate (Na_2WO_4) was dissolved in 75 mL of deionized water and continuously stirred using a magnetic stirrer until a clear and transparent solution was obtained. Once fully dissolved, the stirring was stopped, and concentrated hydrochloric acid (analytical grade) was gradually added. The solution rapidly turned into a yellow suspension. Subsequently, 0.15 g of potassium sulfate (K_2SO_4) was introduced as a reaction promoter, and the mixture was stirred for an additional 2 h to ensure thorough mixing and reaction. The resulting yellow suspension was then transferred into a 100 mL Teflon-lined stainless steel autoclave and subjected to hydrothermal treatment at different temperatures for 24 h. The autoclave was allowed to cool naturally to room temperature after the reaction was completed. The precipitates were collected and washed twice with deionized water and ethanol by centrifugation to remove residual impurities. Finally, the obtained powders were dried in an oven at 60 °C for 6 h and subsequently ground to obtain the final powder samples for further characterization.

Synthesis-representative chemical steps,

(1) Acidification of tungstate precursor: $Na_2WO_4 + 2\ HCl = H_2WO_4 + 2\ NaCl$

(2) Hydrothermal reaction to form WO_3: $H_2WO_4 \xrightarrow{24\ h\ 160\ ^\circ C} WO_3 \cdot nH_2O \xrightarrow{6\ h\ 60\ ^\circ C} WO_3 + nH_2O$

(3) Er-doping Using $ErCl_3 \cdot 6H_2O$ as Er source $(1-x)\ H_2WO_4 + x\ ErCl_3 \cdot 6H_2O \xrightarrow{24\ h\ 160\ ^\circ C} Er_xW_{1-x}O_3 +$ soluble byproducts (e.g., NaCl, H_2O)

The obtained pristine and Er-doped WO_3 powders were subsequently subjected to structural, morphological, optical, and photochromic characterizations, the results of which are presented and discussed in the following sections.

Characterization methods

The crystalline structure of the synthesized products was analyzed using X-ray diffraction (XRD) with a MiniFlex600 diffractometer. The measurements were conducted at a working voltage of 40 kV and a current of 40 mA, with a scanning rate of $0.01°\ s^{-1}$ over a 2θ range of 10° to 70°. The surface morphology of the powders was examined using scanning electron microscopy (SEM, model JSM-7001F) and transmission electron microscopy (Cs-S/TEM, FEI Titan, American). The compositions of the samples were determined through electron probe microanalysis. Both pure WO_3 powders and Er-doped WO_3 samples synthesized *via* the hydrothermal method were subjected to morphological analysis. The agglomeration of the nano-sized tungsten oxide powders was reduced by dispersing a small amount of the sample in ethanol and subjecting it to ultrasonication for 2 min to ensure uniform dispersion. A few drops of the resulting suspension were deposited onto the sample holder and air-dried. Notably, SEM characterization was performed only after the complete evaporation of ethanol. The optical properties of the rare-earth-doped powders were measured using a UV-vis-NIR spectrophotometer (UV-3600 Plus, Shimadzu) in the wavelength range of 300–800 nm. $BaSO_4$ was used as a baseline reference for reflectance calibration during the measurements.

Results and discussion

Initially, the effect of hydrochloric acid concentration on the structure of WO_3 powders was examined. Herein, WO_3 powders were synthesized under the conditions of 180 °C and a reaction

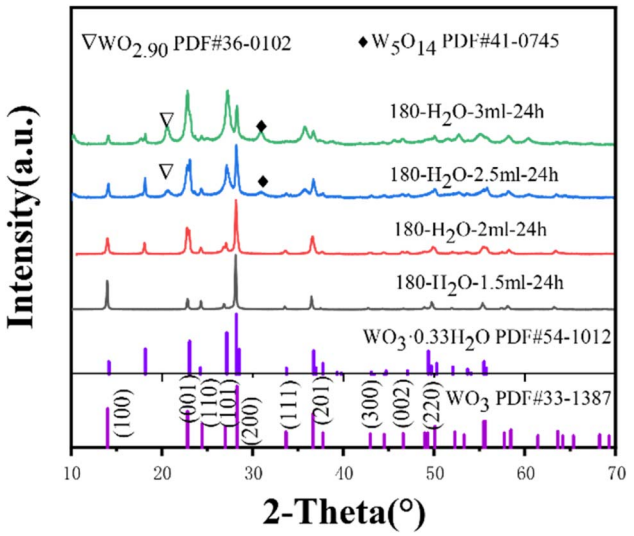

Fig. 1 XRD patterns of WO_3 powders synthesized under different hydrochloric acid concentrations (1.5, 2, 2.5, 3 mL).

time of 24 hours, using solutions with varying hydrochloric acid concentrations (1.5 mL, 2 mL, 2.5 mL, 3 mL). Fig. 1 displays the X-ray diffraction (XRD) patterns of the resulting WO_3 powders. The XRD patterns revealed the significant impact of hydrochloric acid concentration on the purity of the WO_3 powders. Notably, no secondary phases were detected at hydrochloric acid concentrations of 1.5 mL, with all diffraction peaks corresponding to the hexagonal WO_3 phase (PDF#33-1387, *P6/mmm*). However, with increasing hydrochloric acid concentration, the diffraction peaks corresponding to second phases gradually appeared in the WO_3 powder. Moreover, the intensity and number of these second-phase peaks increased with the hydrochloric acid concentration. In the hydrothermal synthesis of WO_3, the reaction temperature is crucial in determining the phase composition, crystallite size, and morphology of the resulting powders. Hence, it is considered one of the most significant influencing factors in the synthesis process. As illustrated in Fig. 2, the morphology of WO_3 powders changes significantly with varying HCl concentrations. At a concentration of 1.5 mL (Fig. 2a), uniform needle-like structures are observed, indicating favorable anisotropic growth. Upon increasing the concentration to 2.0 mL (Fig. 2b), partial aggregation and morphology distortion were observed. Nevertheless, the structure evolved into irregular flake-like particles with rough surfaces at an HCl concentration of 2.5 mL (Fig. 2c). A further increase to 3.0 mL (Fig. 2d) resulted in granular, aggregated particles with reduced uniformity. These results suggest that moderate acid concentration (1.5 mL) is optimal for achieving well-defined nanostructures.

To investigate the effect of reaction temperature on WO_3 synthesis, hydrothermal treatments were conducted at 140 °C, 160 °C, 180 °C, and 200 °C, while keeping other parameters constant. The XRD patterns in Fig. 3 demonstrate that the crystallinity and phase composition of WO_3 are strongly dependent on temperature. The optimal hexagonal phase is obtained at 160 °C, while deviations from this temperature lead to phase impurities or structural transitions. Fig. 4 illustrates that the morphology of the WO_3 powders varies significantly with hydrothermal synthesis temperature. The grains gradually

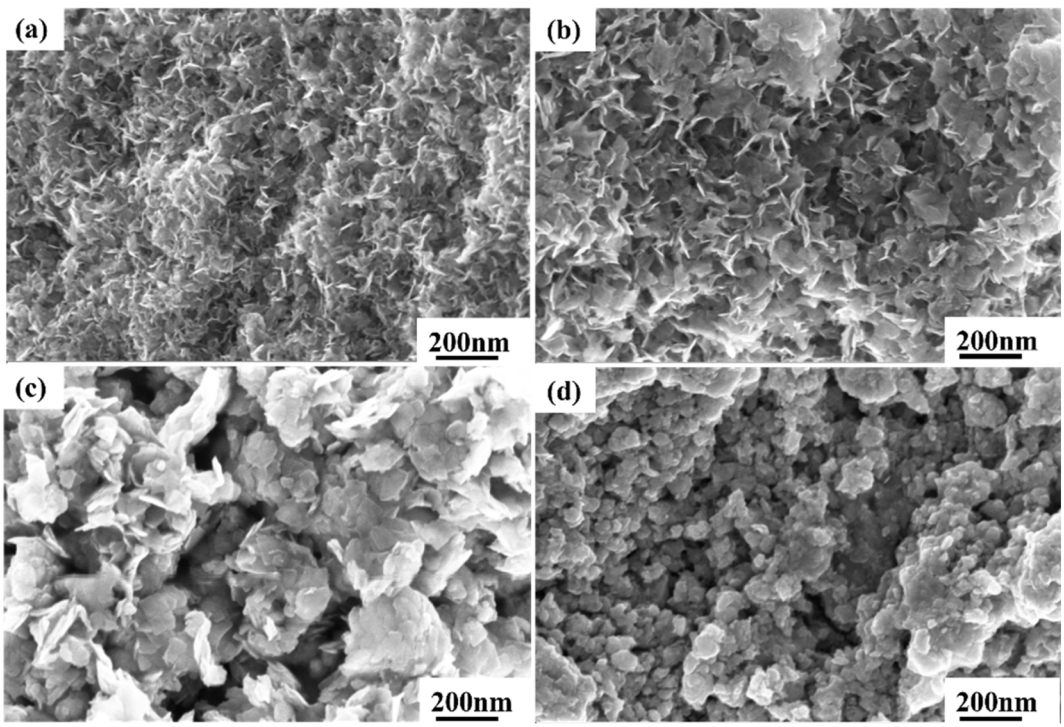

Fig. 2 Morphologies of WO_3 powders synthesized under different hydrochloric acid concentrations. (a) 1.5 mL, (b) 2 mL, (c) 2.5 mL, (d) 3 mL.

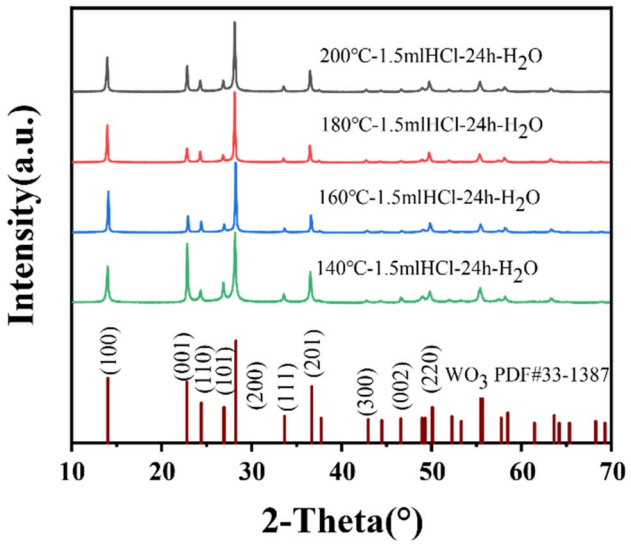

Fig. 3 XRD patterns of WO_3 powders synthesized at different temperatures. (140, 160, 180, 200 °C).

grow as the temperature increases to 140 °C, and most of the urchin-like structures transform into rod-like particles. However, at this stage, the rods are aggregated and show poor dispersion (Fig. 4a). The rod-like grains further grow on further increasing the temperature to 160 °C, and the previously aggregated structures become well-dispersed, distributing uniformly throughout the sample (Fig. 4b). As the temperature reaches 180 °C, the rod-like grains become shorter and thicker, accompanied by the appearance of small particles (Fig. 4c). The rods elongate further at 200 °C, with needle-like structures beginning to form alongside them (Fig. 4d). Meanwhile, 160 °C provides an optimal environment for controlled recrystallization, yielding uniform rods that subsequently serve as structural motifs. The introduction of Er^{3+} disrupts the preferred oriented growth directions by adsorbing onto high-energy facets, which promotes lateral attachment and crosslinking between nanorods. As a result, the material gradually evolves into an interconnected, high-surface-area network capable of improving light-matter interactions and carrier transport.

Although optimizing the hydrothermal conditions effectively improved the phase purity and morphology of WO_3 powders, the intrinsic photochromic performance remained limited. To further enhance the optical response and accelerate the photochromic kinetics, erbium (Er), a rare earth element distinguished by its unique electronic structure and photoactive behavior, was introduced as a dopant. Notably, Er doping is expected to modulate the electronic environment of WO_3, promote charge separation, and facilitate the reversible transition between W^{6+} and W^{5+} states, thereby improving the overall photochromic performance. Fig. 5 presents the XRD patterns of WO_3 powders with varying Er doping concentrations. It was observed that Er doping significantly affected the phase composition of WO_3. At an Er doping molar ratio of 0.01, all diffraction peaks are indexed to the hexagonal phase of WO_3 (PDF#33-1387, space group *P6/mmm*), and no secondary phases are detected. However, the broadening of the diffraction peaks indicates that the introduction of Er^{3+} reduces the crystallite size. The WO_3 phase transforms from the hexagonal phase to a monoclinic phase (PDF#20-1323) as the Er doping

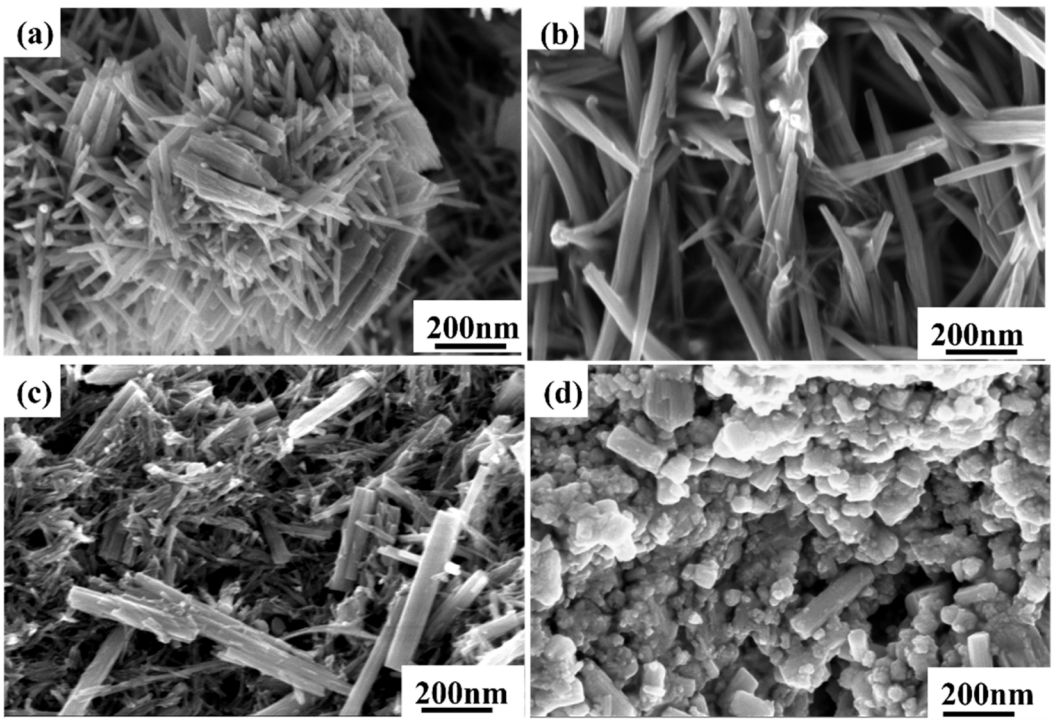

Fig. 4 Morphologies of WO_3 powders synthesized at different temperatures: (a) 140 °C; (b) 160 °C; (c) 180 °C; (d) 200 °C.

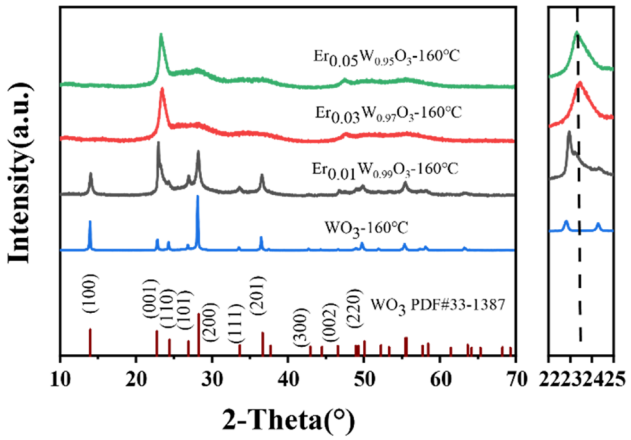

Fig. 5 XRD patterns of WO_3 powders with different Er doping concentrations. (WO_3, $Er_{0.01}W_{0.99}O_3$, $Er_{0.03}W_{0.97}O_3$, $Er_{0.05}W_{0.95}O_3$).

concentration increases to 0.03. Notably, the WO_3 powders maintain this monoclinic structure at a doping concentration of 0.05. The ionic radii of W^{6+} and Er^{3+} are 0.62 Å and 0.881 Å, respectively. Therefore, the substitution of W^{6+} with the larger Er^{3+} ions induces lattice expansion, shifting the diffraction peaks toward lower angles. At a doping level of 3 mol%, the displacement of tungsten atoms from the center to the edge of the unit cell promotes the structural transformation from hexagonal to monoclinic WO_3.

Fig. 6 presents the SEM images of samples with different Er concentrations, illustrating the effect of Er doping on the structure and morphology of WO_3 powders. As shown in Fig. 6, Er doping significantly alters the growth process and leads to the formation of an interconnected, neural network-like morphology. Fig. 6a shows the morphology of pristine WO_3 synthesized at a hydrochloric acid concentration of 1.5 mL and a hydrothermal temperature of 160 °C. The product primarily consists of elongated rod-like particles. The rod-like structures are replaced by irregular needle-like morphologies upon doping with 1 mol% Er (Fig. 6b). Moreover, the average grain size is noticeably reduced. The particles begin to interconnect as the Er doping concentration increases to 3 mol% (Fig. 6c) and form a loosely entangled neural network-like structure. This network-like morphology becomes more pronounced when the Er doping level reaches 5 mol% (Fig. 6d), with the particles coalescing into a continuous and highly disordered interconnected structure. The morphology of WO_3 nano powder changes with controlled synthesis parameter. Especially, with the increasing of Er doping contents, the morphology of WO_3 nano powder changed from rod-like to neural network-like, even the formation mechanism of the neural network-like structure is not clear, but the possible reason may be the Er doping changed the surface energy of WO_3 powders and/or the ripening process during the hydrothermal synthesis where the nanorods are connected with each other and become neural network-like structure. The neural network-like morphology was pursued to increase surface area, facilitate light harvesting, and promote charge separation, which are highly beneficial for photochromic and photocatalytic applications.

Fig. 7 shows the TEM characterizations of the WO_3 nanorods. The low-magnification TEM image (Fig. 7a) reveals that the sample is composed of uniformly distributed WO_3

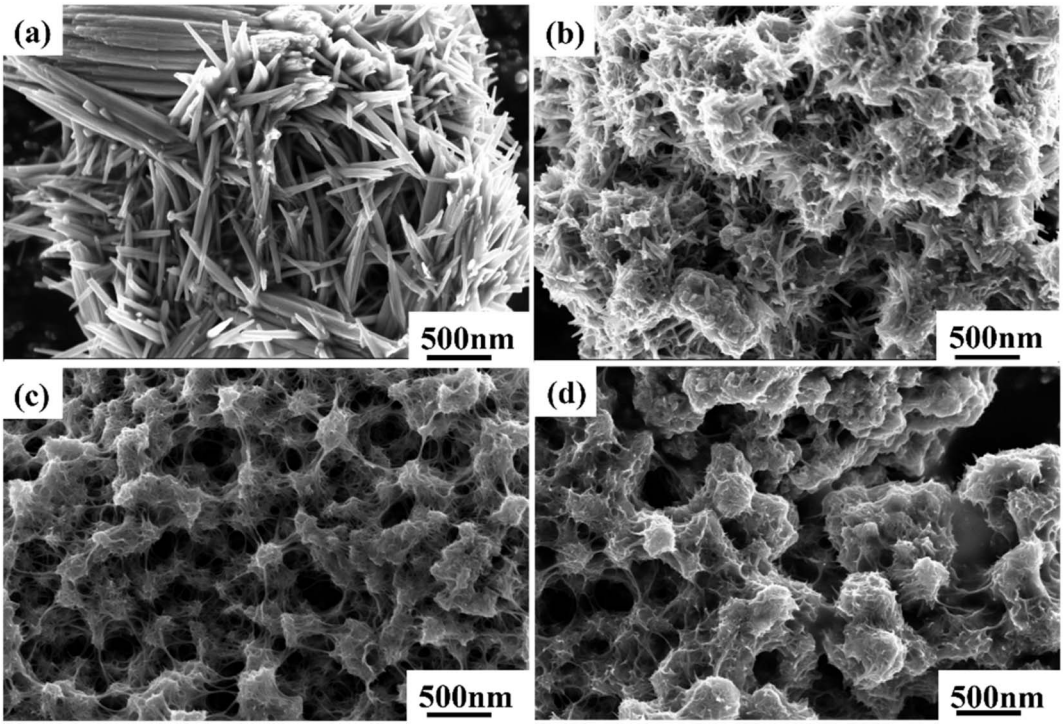

Fig. 6 SEM images of WO_3 powders synthesized with different Er doping concentrations: (a) WO_3 (b) $Er_{0.01}W_{0.99}O_3$ (c) $Er_{0.03}W_{0.97}O_3$ (d) $Er_{0.05}W_{0.95}O_3$.

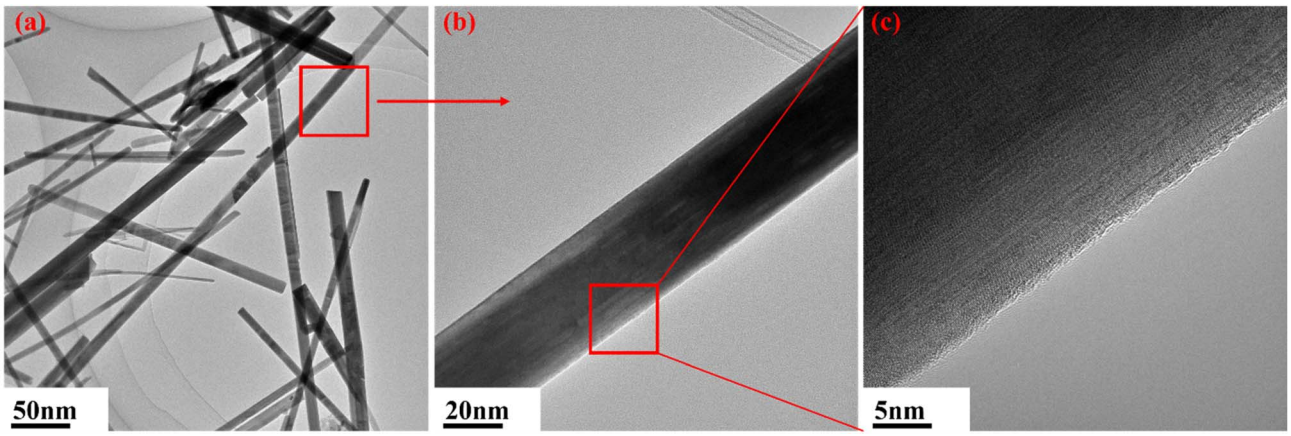

Fig. 7 TEM images of WO_3. (a) Low-resolution image; (b and c) high-resolution image.

nanorods with smooth surfaces and lengths reaching several micrometers. The enlarged image (Fig. 7b) presents the well-defined morphology of an individual nanorod. The high-resolution TEM image (Fig. 7c) displays distinct lattice fringes along the nanorod surface, demonstrating the high crystallinity of the WO_3 nanorods. Fig. 8 presents the TEM analysis of the Er-doped sample $Er_{0.03}W_{0.97}O_3$, providing insights into its microstructure. The low-magnification TEM image in Fig. 8a reveals a loose and entangled network-like morphology formed by interconnected nanorods or nanosheets. The high-resolution TEM image (Fig. 8b) highlights the well-resolved lattice fringes, suggesting the high crystallinity of the sample. Fig. 8c displays the inverse fast Fourier transform (IFFT) of the selected region, revealing distinct lattice fringes with an interplanar spacing of approximately 0.3927 nm, which can be indexed to the (002) planes of monoclinic WO_3. Fig. 8d presents the corresponding selected area electron diffraction (SAED) pattern taken along the [$\bar{1}$11] zone axis, exhibiting clear diffraction spots indexed to the (−202), (022), and (211) planes. This confirms the good crystallinity and the preserved monoclinic phase of WO_3 upon Er doping.

The results clearly show that its morphology gradually evolves from the initial rod-like structure into a neural-network-like architecture, which is consistent with the morphological transition observed in the Er-doped samples. This demonstrates that the structural evolution is universal and reproducible, thereby further supporting the morphology-regulation mechanism proposed in the manuscript. With these additional data, the evidence chain for the morphological transition has been strengthened, and the correlation between structural features and the photochromic behavior has been more clearly established. The incorporation of Er^{3+} into the WO_3 lattice plays a decisive role in reshaping the structural, electronic, and photochromic behavior of the resulting materials. Because Er^{3+} possesses a substantially larger ionic radius than W^{6+}, its partial substitution generates tensile distortion within the [WO_6] octahedra, leading to lattice expansion, peak shifts to lower diffraction angles, and a reduction in crystallite size. When the doping concentration reaches 3 mol%, the accumulated strain further drives the lattice to transform from the hexagonal phase into the monoclinic phase. This distortion offers extra local relaxation pathways that promote electron localization and,

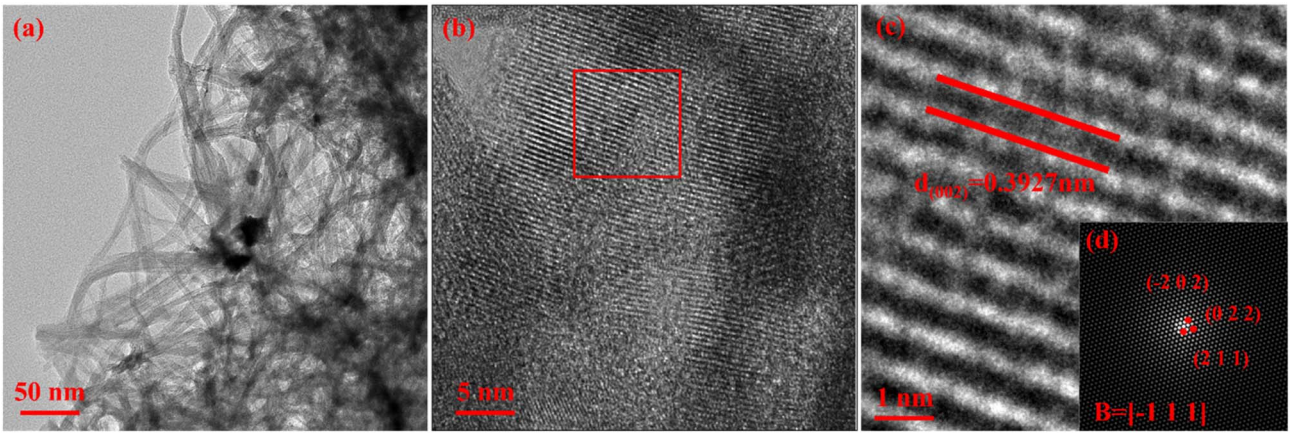

Fig. 8 TEM images of $Er_{0.03}W_{0.97}O_3$. (a) Low-resolution image; (b) high-resolution image; (c) inverse Fourier transform (IFT) of the selected area in (b), with the inset showing the corresponding Fourier transform (FT); (d) select electron diffraction.

consequently, facilitate the formation of W^{5+} centers responsible for photochromic coloration. The morphological evolution from rod-like particles to a neural-network-like architecture originates from the collective effects of solution acidity, reaction temperature, and Er ion participation. With increasing HCl concentration, nucleation and dissolution–recrystallization dynamics shift, altering the balance between anisotropic and isotropic growth.

Fig. 9 shows the optical properties of pure and Er-doped WO_3 samples. As illustrated in Fig. 9a, all samples exhibit strong absorption in the UV region and a clear absorption edge in the visible range. With increasing Er content, the absorption edge gradually shifts toward longer wavelengths (redshift), indicating enhanced visible-light absorption. This phenomenon suggests that Er doping effectively narrows the optical bandgap of WO_3. To further evaluate the band structure, Tauc plots based on the $(\alpha h\nu)^2$ method was constructed, as shown in Fig. 9b. The calculated optical bandgaps for WO_3, $Er_{0.01}W_{0.99}O_3$, $Er_{0.03}W_{0.97}O_3$, and $Er_{0.05}W_{0.95}O_3$ are 2.81 eV, 2.78 eV, 2.76 eV, and 2.75 eV, respectively. This gradual decrease in bandgap energy with increasing Er doping is attributed to the introduction of localized states within the band structure, which facilitates enhanced light absorption in the visible region. These results confirm that rare-earth element doping is an effective strategy for tailoring the electronic structure and optical response of WO_3-based materials. These structural and electronic modifications work synergistically to accelerate the photochromic response. The substitution of W^{6+} with Er^{3+} increases the concentration of oxygen vacancies due to charge compensation, providing a larger number of active sites for electron capture and W^{5+} formation. At the same time, shallow Er-related trap states stabilize photoexcited electrons and slow their recombination with holes, while the interconnected network morphology facilitates faster carrier migration and more efficient utilization of incident photons. Together, these effects enable Er-doped WO_3 to begin coloring within approximately forty seconds, markedly faster than pristine WO_3, and to exhibit stronger and more stable photochromic behavior.

In parallel, Er^{3+} profoundly alters the electronic structure of WO_3. The presence of Er-related 4f states introduces localized energy levels within the bandgap, resulting in a measurable narrowing of the optical bandgap from 2.81 to 2.75 eV. This modification simultaneously enhances visible-light absorption and enables more efficient electron trapping under illumination. Because these Er-induced trap states prolong the carrier lifetime and reduce the activation barrier for the W^{6+}/W^{5+} redox process, the system more readily accumulates photoexcited electrons, intensifying the generation of blue W^{5+}–O centers. Overall, Er^{3+} simultaneously induces lattice distortion, introduces 4f-mediated intermediate states, enhances oxygen-vacancy formation, and redirects crystal-growth pathways. These interconnected mechanisms collectively yield a material with tunable structural characteristics, modified band structure, and significantly accelerated photochromic switching, providing a coherent and comprehensive understanding of the enhanced performance observed in Er-doped WO_3 systems.

To evaluate the impact of Er doping on the photochromic behavior of WO_3, visual color changes under UV irradiation were recorded and compared across all samples. Fig. 10 displays the color change of all WO_3 samples before and after 30 minutes of UV exposure. Notably, the pure WO_3 powder transitions from light gray to dark blue upon irradiation. However, the Er-doped yellow WO_3 powders develop a blue hue within 40 seconds of UV exposure, and turn completely dark blue after 15 minutes, reflecting a significantly faster and more pronounced photochromic response than the undoped sample. However, the photochromic effect weakens as the Er doping concentration reaches 5%. This is likely caused by excessive doping, which induces a phase transformation that suppresses photochromic behavior. Notably, the WO_3 powders doped with 1% and 3% Er gradually shift in color from yellow to cyan green under natural light, suggesting that Er doping lowers the energy threshold required for excitation and improves light sensitivity. Moreover, the photochromically colored WO_3 powders were thermally annealed to assess their reversibility following exposure. Furthermore, the sample doped with 1% Er exhibited partial

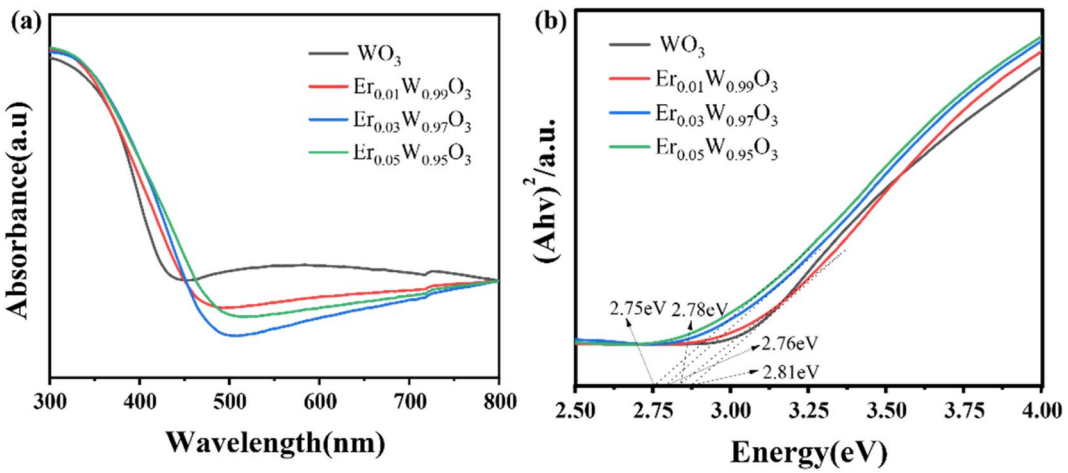

Fig. 9 (a) UV-vis absorption spectra of pure WO_3 and Er-doped WO_3 samples with different doping concentrations. (b) Tauc plots for estimating the optical bandgap energy of the samples, showing a gradual reduction in bandgap with increasing Er content.

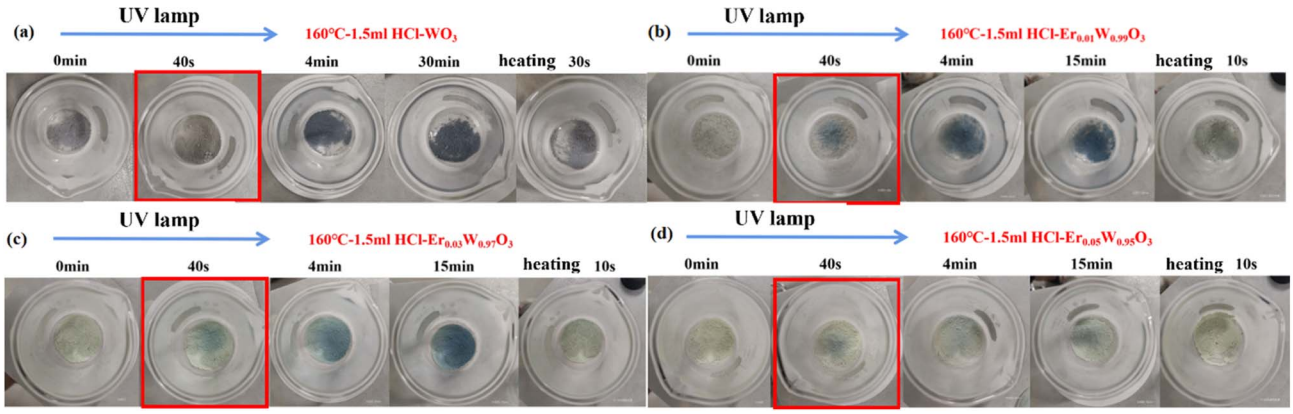

Fig. 10 HCl-treated Er-doped WO_3 under UV irradiation and heating images of (a) WO_3, (b) $Er_{0.01}W_{0.99}O_3$, (c) $Er_{0.03}W_{0.97}O_3$, and (d) $Er_{0.05}W_{0.95}O_3$ after UV exposure.

recovery of the original color after heating, although the photochromic contrast diminished with repeated cycles. Notably, the sample with 3% Er doping demonstrated the most distinct and stable photochromic effect, with minimal color loss after thermal reduction and requiring the shortest recovery time. Upon Er^{3+} doping into WO_3, its 4f orbitals form localized intermediate electron energy levels positioned between the valence band and conduction band. Due to the highly localized nature of 4f electrons, these intermediate levels can serve as transition states for electron transitions, thereby reducing the material's effective bandgap and enhancing visible light absorption. In other words, when the photon energy is below the original bandgap, electrons can still transition from the valence band to the conduction band *via* the 4f states. Simultaneously, Er^{3+} doping induces oxygen vacancy formation to maintain charge balance. As shallow-level defects, oxygen vacancies trap electrons and stabilize localized W^{5+} states. This localized electron trapping not only further modulates the mater/electronic structure but also accelerates photogenerated electron–hole separation and the $W^{6+} \rightarrow W^{5+}$ reduction process. A synergistic effect emerges between oxygen vacancies and the Er^{3+} 4f state: the 4f state provides additional electron transition pathways, while oxygen vacancies stabilize and localize electrons. This ultimately leads to a narrowed bandgap, enhanced visible light absorption, and more efficient electron–hole separation and W^{6+} reduction.

Conclusion

In summary, this study presents the successful synthesis of a uniform and morphology-controlled WO_3 neural network-like structure *via* a hydrothermal method under optimized conditions of 160 °C for 24 h. The introduction of rare earth dopants was found to significantly influence the structural and optical properties of WO_3. In particular, Er doping effectively narrowed the bandgap and enhanced light absorption, with the $Er_{0.03}W_{0.97}O_3$ composition exhibiting the most favorable optical characteristics among all samples. Remarkably, rare earth element doping is an effective strategy in tailoring the photochromic behavior of WO_3, with $Er_{0.03}W_{0.97}O_3$ composition exhibiting the most enhanced photochromic performance among all samples. These findings provide valuable insights into the controllable design and electronic structure modulation of WO_3-based nanomaterials, paving the way for their potential applications in photocatalysis and other optoelectronic fields.

Author contributions

Ran Tian: investigation, writing – original draft, methodology. Yu-Qiang An: methodology, investigation. Ze-Yuan Yang: supervision, methodology. Xing Yang: methodology, investigation. Zhen-Hua Ge: writing – review & editing, supervision, funding acquisition.

Conflicts of interest

The authors declare that they have no known competing financial interests or personal relationships that could have appeared to influence the work reported in this paper.

Data availability

All data supporting the findings of this study are available within the article.

Acknowledgements

This work was supported by the Academician (Expert) Workstation of Yunnan Province Program (grant no. 202405AF140066), Yunnan Science and Technology Program (202401AT070403), Outstanding Youth Fund of Yunnan Province (grant no. 202201AV070005), National Key R&D Program of China (no. 2022YFF0503804), National Natural Science Foundation of China (grant no. 52162029), Yunnan Major Scientific and Technological Projects (grant no. 202302AG050010).

References

1 N. Yuan, D.-Y. Liu, X.-C. Yu, H.-X. Sun, C.-G. Ming, W.-H. Wong, F. Song, D.-Y. Yu, E. Y.-B. Pun and D.-L. Zhang, A Biological Nano-Thermometer Based on Ratiometric Luminescent Er^{3+}/Yb^{3+}-Co doped $NaGd(WO_4)_2$ Nanocrystals, *Mater. Lett.*, 2018, **218**, 337–340, DOI: 10.1016/j.matlet.2018.02.007.

2 Y. Jia, C. Yang, X. Chen, W. Xue, H. J. Hutchins-Crawford, Q. Yu, P. D. Topham and L. Wang, A Review on Electrospun Magnetic Nanomaterials: Methods, Properties and Applications, *J. Mater. Chem. C*, 2021, **9**, 9042–9082, DOI: 10.1039/D1TC01477C.

3 M. Y. Sun, F. Y. Bai, Q. L. Guan, Y. H. Xing and F. Xu, Construction of Naphthalene Diimide-Based Cadmium Complexes and Their Application in Iodine Adsorption, Photochromism, and Photocatalysis, *CrystEngComm*, 2022, **24**, 8309–8320, DOI: 10.1039/D2CE01192A.

4 Y. Kajiwara and H. Nakai, Crystal Polymorphism and Crystalline-State Photochromism of a Rhodium Dithionite Complex with *n* -Methoxypropyl Moieties, *CrystEngComm*, 2022, **24**, 1437–1441, DOI: 10.1039/D1CE01613J.

5 L. Belhomme, M. Gaudon and S. Ravaine, Effect of Dissolved O_2 on the Photochromism of Suspended WO_3 Nanoparticles, *J. Phys. Chem. C*, 2025, **129**, 10240–10248, DOI: 10.1021/acs.jpcc.5c00852.

6 C. Kim, V. Lokhande, D. Youn and T. Ji, Electrochromism in Hf-Doped WO_3, *J. Solid State Electrochem.*, 2022, **26**, 1557–1566, DOI: 10.1007/s10008-022-05187-x.

7 X. Liu, X. Jia, M. Fischer, Z. Huang and D. R. Smith, Enhanced Two-Photon Photochromism in Metasurface Perfect Absorbers, *Nano Lett.*, 2018, **18**, 6181–6187, DOI: 10.1021/acs.nanolett.8b02042.

8 L. Liu, L.-T. Zhang, F.-C. Yuan, H.-X. Ren, Y. Ma and Q.-L. Wang, Extended Viologen Compounds with Photochromism, Photoresponsive Luminescence and Ultrahigh Quenching Efficiency, *CrystEngComm*, 2024, **26**, 4431–4438, DOI: 10.1039/D4CE00615A.

9 A. K. Nayak, Y. Sohn and D. Pradhan, Facile Green Synthesis of $WO_3 \cdot H_2O$ Nanoplates and WO_3 Nanowires with Enhanced Photoelectrochemical Performance, *Cryst. Growth Des.*, 2017, **17**, 4949–4957, DOI: 10.1021/acs.cgd.7b00886.

10 X. Dong, Y. Shao, X. Ren, Z. Li, K. Li, Y. Tong, X. Liu and Y. Lu, Inserting Bi Atoms on the $[WO_6]$ Framework: Photochromic WO_3/Bi_2WO_6 Nanoparticles Enable Visual Sunlight UV Sensing, *Appl. Surf. Sci.*, 2023, **636**, 157783, DOI: 10.1016/j.apsusc.2023.157783.

11 S. Hou, Y. Zou, X. Liu, X. Yu, B. Liu, X. Sun and Y. Xing, CaF_2 and CaF_2 :Ln^{3+} (Ln = Er, Nd, Yb) Hierarchical Nanoflowers: Hydrothermal Synthesis and Luminescent Properties, *CrystEngComm*, 2011, **13**, 835–840, DOI: 10.1039/C0CE00396D.

12 X. Zhao, Z. Yang, X. Yang, R. Wang, M. Yuan, K. Han, Z. Jiang, H. Wang and X. Xu, Controlling the Multicolor Upconversion Luminescence in CaF_2 Nanocrystals Doped with Yb^{3+}, Er^{3+} and Nd^{3+} Ions under the Excitation of a 808 Nm Laser, *Opt. Mater. Express*, 2019, **9**, 4578, DOI: 10.1364/OME.9.004578.

13 A. T. Smith, H. Ding, A. Gorski, M. Zhang, P. A. Gitman, C. Park, Z. Hao, Y. Jiang, B. L. Williams, S. Zeng, *et al.*, Multi-Color Reversible Photochromisms via Tunable Light-Dependent Responses, *Matter*, 2020, **2**, 680–696, DOI: 10.1016/j.matt.2019.12.006.

14 L. L. Liu, D. Zhu, L. L. Cao and D. W. Stephan, N-Heterocyclic Carbene Stabilized Parent Sulfenyl, Selenenyl, and Tellurenyl Cations (XH^+ , X = S, Se, Te), *Dalton Trans.*, 2017, **46**, 3095–3099, DOI: 10.1039/C7DT00186J.

15 S. Crespi, N. A. Simeth, M. Di Donato, S. Doria, C. N. Stindt, M. F. Hilbers, F. L. Kiss, R. Toyoda, S. Wesseling, W. J. Buma, *et al.*, Phenylimino Indolinone: A Green-Light-Responsive T-Type Photoswitch Exhibiting Negative Photochromism, *Angew. Chem., Int. Ed.*, 2021, **60**, 25290–25295, DOI: 10.1002/anie.202111748.

16 C. Bechinger, E. Wirth and P. Leiderer, Photochromic Coloration of WO_3 with Visible Light, *Appl. Phys. Lett.*, 1996, **68**, 2834–2836, DOI: 10.1063/1.116340.

17 O. Oms, T. Benali, J. Marrot, P. Mialane, M. Puget, H. Serier-Brault, P. Deniard, R. Dessapt and A. Dolbecq, Fully Oxidized and Mixed-Valent Polyoxomolybdates Structured by Bisphosphonates with Pendant Pyridine Groups: Synthesis, Structure and Photochromic Properties, *Inorganics*, 2015, **3**, 279–294, DOI: 10.3390/inorganics3020279.

18 P.-E. Car and G. R. Patzke, The Fascination of Polyoxometalate Chemistry, *Inorganics*, 2015, **3**, 511–515, DOI: 10.3390/inorganics3040511.

19 C. Avellaneda and L. Bulhões, Photochromic Properties of WO_3 and WO_3:X (X=Ti, Nb, Ta and Zr) Thin Films, *Solid State Ionics*, 2003, **165**, 117–121, DOI: 10.1016/j.ssi.2003.08.023.

20 Y. Badour, V. Jubera, I. Andron, C. Frayret and M. Gaudon, Photochromism in Inorganic Crystallised Compounds, *Opt. Mater.:X*, 2021, **12**, 100110, DOI: 10.1016/j.omx.2021.100110.

21 F.-X. Sun, A. Gao, B.-Y. Yan, J. Zhang, X.-R. Wang, H.-J. Zhang, D.-C. Dai, Y.-H. Zheng, X. Deng, C. Wei, D.-S. Wang, *et al.*, Self-Adaptive Photochromism, *Sci. Adv.*, 2024, **10**, eads2217, DOI: 10.1126/sciadv.ads2217.

22 Z.-G. Zhao, Z.-F. Liu and M. Miyauchi, Tailored Remote Photochromic Coloration of in Situ Synthesized CdS Quantum Dot Loaded WO_3 Films, *Adv. Funct. Mater.*, 2010, **20**, 4162–4167, DOI: 10.1002/adfm.201001198.

23 J.-H. Li, S.-D. Han, J. Pan, Z.-Z. Xue, G.-M. Wang, Z.-H. Wang and Z.-Z. Bao, Template Synthesis and Photochromism of a Layered Zinc Diphosphonate, *CrystEngComm*, 2017, **19**, 1160–1164, DOI: 10.1039/C7CE00212B.

24 X. Li, W. Zheng and Y. Zhang, The Making and Breaking of Perovskite Photochromism through Doping, *Nanoscale*, 2022, **14**, 12574–12580, DOI: 10.1039/D2NR03931A.

25 Q. Li, H. Zhang, Y. Yan, Z. Yang, Y. Wang, G. Liu and T. Ni, Tunable and Sustainable Photocatalytic Activity of Photochromic Y-WO_3 under Visible Light Irradiation, *RSC Adv.*, 2021, **11**, 1147–1152, DOI: 10.1039/D0RA09714D.

26 F. Qu, B. He, R. Guarecuco and M. Yang, Mesoporous WN/WO_3-Composite Nanosheets for the Chemiresistive Detection of NO_2 at Room Temperature, *Inorganics*, 2016, **4**, 24, DOI: 10.3390/inorganics4030024.

27 L. Carmel, S. Aharon, D. Meyerstein, Y. Albo, L. Friedlander, D. Shamir and A. Burg, WO_3 Dehydration and Phase Transition as the Catalytic Driver of Hydrogen Production by Non-Calcinated WO_3, *Int. J. Hydrogen Energy*, 2024, **51**, 1508–1520, DOI: 10.1016/j.ijhydene.2023.07.351.